



Enhancing the performance of supercapacitor electrode from chemical activation of carbon nanofibers derived *Areca catechu* husk via one-stage integrated pyrolysis

Erman Taer¹ · Friska Febriyanti¹ · Widya Sinta Mustika¹ · Rika Taslim² · Agustino Agustino¹ · Apriwandi Apriwandi¹

Received: 4 June 2020 / Revised: 24 August 2020 / Accepted: 19 September 2020 / Published online: 3 October 2020
© Korean Carbon Society 2020

Abstract

A carbon nanofiber was produced from the *Areca catechu* husk as a supercapacitor electrode, utilizing a chemical activation of potassium hydroxide (KOH) at different concentrations. One-stage integrated pyrolysis both carbonization and physical activation were employed for directly converting biomass to activated carbon nanofiber. The morphology structure, specific surface area, pore structure characteristic, crystallinity, and surface compound were characterized to evaluate the influence on electrochemical performance. The electrochemical performance of the supercapacitor was measured using cyclic voltammetry (CV) through a symmetrical system in 1 M H₂SO₄. The results show that the KOH-assisted or absence activation converts activated carbon from aggregate into a unique structure of nanofiber. The optimized carbon nanofiber showed the large specific surface area of 838.64 m² g⁻¹ with the total pore volume of 0.448 cm³ g⁻¹, for enhancing electrochemical performance. Beneficial from its unique structural advantages, the optimized carbon nanofiber exhibits high electrochemical performance, including a specific capacitance of 181.96 F g⁻¹ and maximum energy density of 25.27 Wh kg⁻¹ for the power density of 91.07 W kg⁻¹. This study examines a facile conventional route for producing carbon nanofiber from biomass *Areca catechu* husk in economical and efficient for electrode supercapacitor.

Keywords Activated carbon · *Areca catechu* husk · Carbon nanofiber · Chemically activation · Supercapacitor

1 Introduction

Energy storage has been extensively studied due to the increasing energy consumption in recent years. This has been contributed by the rapid advancements in technology and the digital era, which have necessitated research on high power and energy density, as well as portable device packaging [1]. Additionally, fossil energy needs to be replaced due to depletion sources and their emission [2]. Environmentally friendly and sustainable source for electrical energy storage, such as supercapacitor, can be a solution to these issues. The supercapacitor has high power and energy density, rapid

charging-discharging, long lifetimes, safety, and excellent energy performance [3].

There are two types of supercapacitors based on the ions storage mechanism [4]. First, there is the electrochemical double-layer capacitances (EDLC), where capacitance is the accumulation of ion pairs between electrolyte and surface electrode [5]. The second one is pseudo-capacitance, which has a higher capacitance than EDLC. Its capacitance is the redox reaction generated from the interactions of the surface functionalities with the active species in the electrolyte [6]. However, the redox reaction could be considered corrosive for a current collector and higher resistivity of supercapacitor cells. Both above mentioned features lead to a decrease in power density, low conductivity, and poor cycle stability [7]. Therefore, EDLC is recommended for good cycle stability and electrical conductivity. It is an environmentally device without chemical reaction and electrolyte depletion [8].

To enhance the capacitance of EDLC, many researchers have focused on developing the properties of its electrode since capacitance is proportional to its specific surface area [9]. A large specific surface area promotes a larger active

✉ Erman Taer
erman_taer@yahoo.com

¹ Department of Physics, University of Riau, Simpang Baru, 28293 Riau, Indonesia

² Department of Industrial Engineering, State Islamic University of Sultan Syarif Kasim, Simpang Baru, 28293 Riau, Indonesia

area in contact with the electrolyte for high energy storage [10]. Therefore, activated carbon with high porosity is suitable for EDLC electrodes due to the large surface area [8]. According to the storage mechanism of pure EDLC, activated carbon provides specific surface area and capacitance of 3000 mg^{-2} and 300 F g^{-1} , respectively [11, 12]. Additionally, pore volume and size distribution influence the performance of supercapacitor electrodes. The micropores ($< 2 \text{ nm}$) promote ions storage to generate high energy performance. The mesopores ($2\text{--}50 \text{ nm}$) and macropores ($> 50 \text{ nm}$) reduce the pathway for ion diffusion, leading to rapid mobility and reduced power loss [13]. In summary, large specific surface area and pore size combination are essential factors to be considered in designing activated carbon for supercapacitor electrodes.

Activated carbon with unique structures such as carbon nanofiber is advantageous in charge transfer and allows fast access of electrolyte ions to the surface of the electrodes [14]. Chen et al. (2008), obtained carbon nanofiber from biomass, including palm kernel shell, coconut, and wheat straw, through chemical vapor deposition (CVD) [15]. CVD directly produces carbon nanofiber without dissolving preparation with low fiber density. Moreover, the CVD process needs catalysts and conducted in high vacuum conditions [16]. The electrospinning method has been widely used to produce carbon nanofiber with high specific surface area and fiber density, excellent electrochemical performance, and lower energy process [17]. It is a commonly used polymer precursor, or carbon biomass mixing the polymer, which increases production cost [18]. Electrode production in the two-stage electrospinning process for converting a suspension into fiber and pyrolysis process takes a longer time [19]. Therefore, these methods are uneconomic and inefficient for electrode production.

To cut down the cost of production of the electrode, the biomass waste with nature fiber structure can be used as an alternative for supporting the facile method to produce carbon nanofiber [20]. It is abundant, easy to process, has zero cost, and can be performed in a wide range of temperatures, and providing pore and structure nature [21]. One stage integrated pyrolysis can promote an alternative for a facile method for producing activated carbon nanofiber [22]. Some biomass have been reported to become attractive precursors for activated carbon, including *Rhus typhina* fruits [23], palm oil [24], tea waste [25], pistachio shell [26], rice husk [27], *mangosteen* peels [28], banana peel [29], tree bark [30], lotus leave [31], cotton [32], egg white [33], strobili fibers [20], dandelion [34], dairy manure [35], and wild fungus [36]. Biomass contains a large amount of cellulose, hemicellulose, and lignin, which constitute tissue for pore and structure nature [37–39]. Celluloses can be extracted into nano-sized fiber due to the presence of elemental fibril [34, 40].

Activated carbon from biomass was commonly studied as powder and monolith. Activated carbon powder has a higher specific surface area than a monolith, specifically 2700 mg^{-1} , which increases electrochemical performance [23, 41]. However, it is not widely used due to dusting for further energy storage applications. The additive polymer for supercapacitor assembly leads to a loss of conductivity [42]. It is necessary to use monolith electrodes for good mechanical properties since it can be directly used for packaging. The monolith produces higher electrical conductivity, specific capacitance, and good cycling capability at high current densities [43].

Areca catechu fruit husk, a native of Southeast Asia, is an abundantly cultivated waste material. It is obtained in the range of 60–80% of its total weight and volume of the fresh fruit [44]. Its ripen nut has been used for industrial textile coloring, which produces abundant unutilized husk [45]. It contains cellulose (34.18%), hemicellulose (20.83%), lignin (31.60%), and a few minerals [44]. Based on structure, it is 40% fiber and has a diameter size ranging from $396 \mu\text{m}$ to $476 \mu\text{m}$ [46]. The fiber has a longitudinal arrangement and bonds the microfibril structure [47]. Therefore, *Areca catechu* fruit husks can be used to produce activated carbon nanofibers for the monolith electrode.

This study reports a facile and low-cost method using one stage integrated pyrolysis to produce activated carbon nanofiber from the *Areca catechu* husk (ACH). The samples were prepared using chemical activation of KOH at different concentrations to show the morphology transformation from aggregate into a nanofiber. The activated carbon nanofiber of ACH has the highest specific surface area of $838 \text{ m}^2 \text{ g}^{-1}$ in the concentration of 0.7 M KOH. In a two-electrode cell, the nanofiber structure compared to aggregate remarkably increases the specific capacitance from 101.63 to 181.96 F g^{-1} at a scan rate of 1 mV s^{-1} , in the 1 M H_2SO_4 electrolyte. These results show the great potential of *Areca catechu* fruit husk (ACH) for activated carbon nanofiber as a supercapacitor electrode.

2 Experimental

2.1 Materials and methods

The ripen *Areca catechu* husk (ACH) were collected from Riau province (Riau, Indonesia). The ACH sample was processed into the fiber for raw material preparation. Importantly, chemical materials such as Potassium hydroxide (KOH) and Sulfuric acid (H_2SO_4) were based on Merck KGaA (Darmstadt, Germany). All chemical materials were chosen in the analytical grade and can be used without further purification.

2.2 Sample preparation

The ACH fibers were converted into powder via pre-carbonized and sieved of size of less than 53 μm , following the previous study [48]. ACH powder was treated with KOH at different concentration (0 M, 0.3 M, 0.5 M, 0.7 M, 0.9 M). The samples were labeled ACH-X, where X was the concentration of KOH. All ACH-X were molded into a pellet of diameter ± 2 cm, which was pressed by a hydraulic press. Subsequently, the ACH-X pellets were converted into activated carbon via one-stage integrated pyrolysis both of carbonization (600 $^{\circ}\text{C}$ N_2) and physical activation (900 $^{\circ}\text{C}$ CO_2 for 2.5 h), following the previously study [48]. Finally, the activated carbon from ACH-X pellets was purified using deionized water until neutral PH and polished for electrode supercapacitor preparation.

2.3 Structure characterization

The mass, diameter, and thickness were measured to determine the density of ACH-X pellets before and after the pyrolysis process. The morphology structure of activated carbon from ACH-X pellets was characterized by scanning electron microscopy (SEM) (JEOL-JSM-6510LA) and embedded with energy dispersive x-ray spectroscopy (EDS). Additionally, specific surface area (SSA) was determined using the Brunauer Emmett Teller (BET) adsorption model (Quantachrome TouchWin Version 1.2). The pore size distribution was based on the desorption branch of the isotherms, calculated using the Barrett–Joyner–Halenda (BJH) method. The crystallinity degree of the ACH-X samples was investigated using an X-ray diffractometer (XRD) (X-Pert Powder PW 30/40 and a wavelength of $\text{Cu-K}\alpha$ 15,406 \AA).

2.4 Electrochemical performance evaluation

The pellet based activated carbon of ACH-X was immersed in a liquid electrolyte of 1 M H_2SO_4 for 48 h. Subsequently, the ACH-X pellets were utilized as electrode supercapacitors. They were assembled in the symmetrical layers, which was separated by separator using an duck egg shell. The preparation of separator was explained in detail in the previous work [49]. stainless steel was used as a current collector with the voltage range of 0.0–1.0 V. The symmetric supercapacitor was performed on the CV UR Rad-Er 5841 instrument. It was calibrated to VersaStat II Princeton Applied Research, with an error of $\pm 6.05\%$. The CV measurement was conducted in two electrodes systems, approaching the real utilization of energy storage devices. To investigate the electrochemical performance, the specific capacitance was calculated following the Eq. (1) below.

$$C_{sp} = \frac{I_c - I_d}{m \times s}. \quad (1)$$

The energy and power densities were calculated from CV using the Eq. (2) and (3), respectively.

$$E = \frac{1}{2} C_{sp} \Delta V^2 \times \frac{1000}{3600}, \quad (2)$$

$$P = \frac{E}{\Delta t / 3600}, \quad (3)$$

where C_{sp} is the specific capacitance (F g^{-1}), while I_c and I_d are the charge and discharge current (A), respectively. Also, m is the average mass loading of two electrodes (g) while E is the average energy density of the electrode (Wh kg^{-1}). ΔV and Δt are the potential window of CV (V) and discharge time in the discharge process (s), respectively. P is the average power density of the electrode (W kg^{-1}).

3 Result and discussion

3.1 Density

At high temperature, pyrolysis changes the pellet of the monolith activated carbon from ACH-X. The diameter, thickness, and mass of ACH-X pellets were resumed in the density variable, as shown in Fig. 1. The data was calculated from 10 pellets for each sample, and the results showed pyrolysis reduced density. The carbonization process at the high temperature of 600 $^{\circ}\text{C}$ releases some of the low molecular weight volatiles, such as oxygen, nitrogen, and hydrogen, reducing the mass of the pellets [13]. Besides, the physical activation

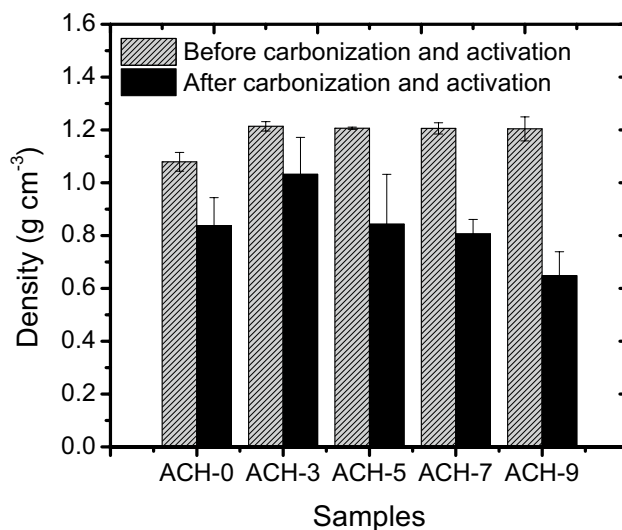


Fig. 1 Density diagram of the activated carbon from ACH-X

of CO₂ produced residues such as carbon monoxide in the gaseous phase [43]. The volatiles released to generate the vacancies in the carbon chains leading to rearrangements that reduced both the pellet diameter and thickness.

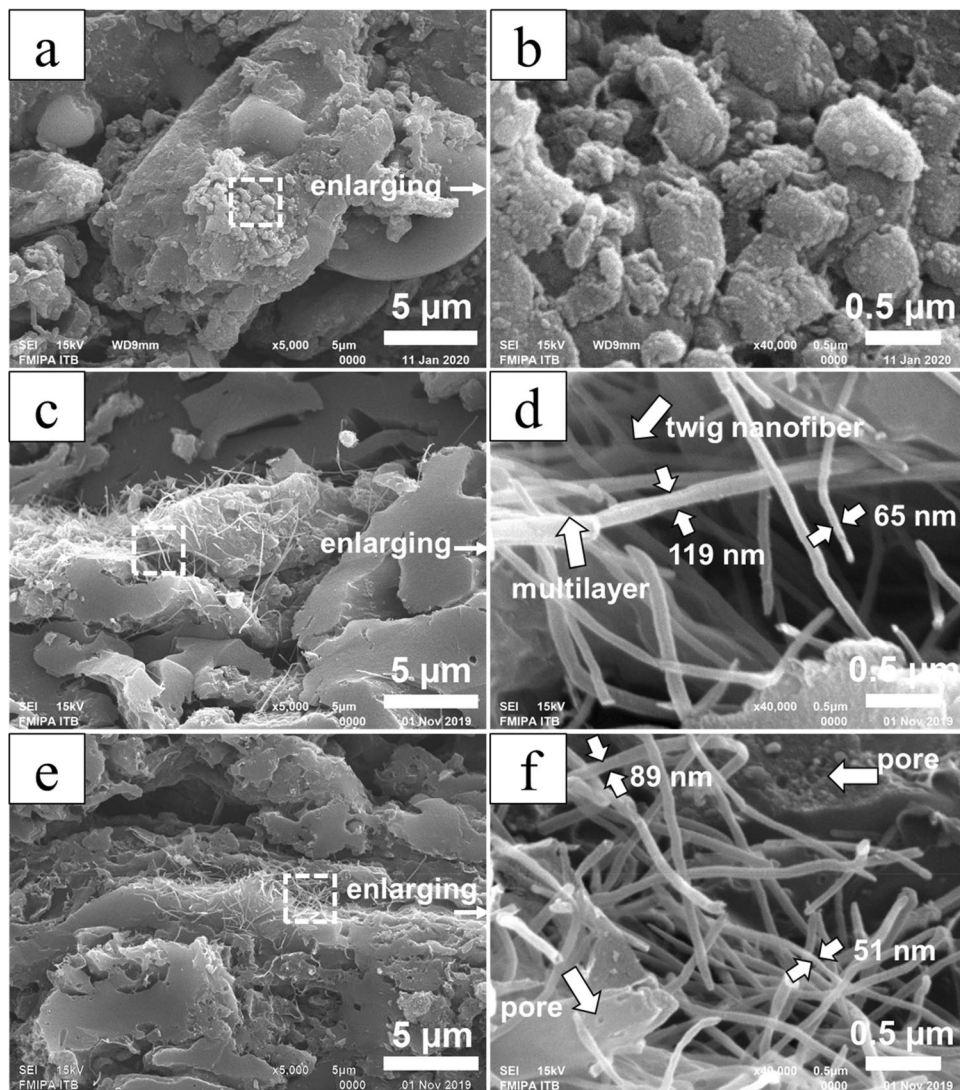
The chemical activating agent of KOH increases the density of the pre-carbonized ACH-X samples before pyrolysis from 1.079 to 1.21 g cm⁻³ for ACH-0 and ACH-3, respectively. This due to impregnate of the higher molecular weight of KOH into carbon biomass. As the concentration of KOH increases, the density remains the same for ACH-3, ACH-5, ACH-7, and ACH-9, specifically 1.21, 1.21, 1.21, 1.20 g cm⁻³. The pellets preparation was conducted at a constant mass, size of the template, and the weight of hydraulic press. It was assumed that there was no significant effect on pellet density before pyrolysis, though the chemical activation influenced the density after the process. Essentially, it shrank at the different ratios, including 22.5%, 14.9%, 30.1%, 33.2%, and 46.2% for ACH-0, ACH-3, ACH-5,

ACH-7, and ACH-9, respectively. The increase in the concentration of KOH raised the new micropores formation [13, 50]. This led to high porosity and specific surface area, which improved electrochemical performance. Therefore, increasing concentration from ACH-7 to ACH-9 decreases the density significantly. It indicates the higher porosity and enlarges the micropores to larger pores [50, 51]. These results indicate that electrochemical performance for ACH-9 reduces as predicted.

3.2 Structural characteristic

As shown in Fig. 2, the morphology of carbon samples was observed by scanning electron microscopy (SEM). The morphology and structure of the activated carbon derived biomass materials was affected by raw materials, activating agent and the treatment to convert it into carbon material [13]. Generally, biomass materials contain cellulose,

Fig. 2 SEM images of samples (a) ACH-0 (b) is the enlarged image of the selected region in (a) (c) ACH-3 (d) is the enlarged image of the selected region in (c) (e) ACH-7 (f) is the enlarged image of the selected region in (e)



hemicellulose, and lignin [37, 38], which have the potential to develop into any structures of carbon materials, including carbon sheet [52], fiber [20], nanotubes [32, 48], and particles [53]. Additionally, they provide natural pores, though the disordered carbon atoms and heteroatoms block them [21, 42]. The KOH activating agent was impregnated into pre-carbonized ACH for fabricating nanofiber and porous carbon. The activation process of KOH was carried out in one stage integrated pyrolysis with both carbonization and physical activation. During the carbonization, the low molecular weight of volatiles such as oxygen, nitrogen and hydrogen changed into the tars and gases [13]. Hence, they were released in the gas phase, leading to carbon atom rearrangement. In addition, the physical activation in the high temperature facilitated pore development through gasification reaction between ACH char and CO₂ [43].

Figure 2 show the SEM image of activated carbon electrode from ACH-x samples. The pelletizing process on synthesis of carbon electrode generated some open pores network between adjacent aggregate of ACH. Figure 2a shows that activated carbon derived from ACH-0 without KOH-impregnated have an aggregate-like structure in size ranging from 3.02 to 4.03 μm. There are some open pores network between the aggregates, though within 0.51–0.97 μm. It is also clear that ACH-0 have various range of aggregates as shown by the marked region in the Fig. 2b. The aggregate size and open pores network ranged from 0.28 to 0.47 μm and 35–84 nm, respectively. Hence, the supramolecular of ACH-0 raw materials decomposed into aggregate structures due to pyrolysis [14]. In the first step, the carbonization process at the temperatures of 600 °C under N₂ decomposes the hemicellulose and cellulose structure [21, 54]. In the second step, the lignin structure in the ACH-0 decomposed due to the physical activation at the temperature 900 °C [14, 38]. Additionally, physical activation achieved the reaction at between a carbon atom of ACH and CO₂ at the surface. This produced the gaseous residue of carbon monoxide, opening inaccessible pores [43]. This further predicts the open pores network of ACH-0 which produce specific surface area and supports ion diffusion into mesopores and micropores.

Meanwhile, KOH activation leads to structural modification on the ACH-3 from large to small aggregate and nanofiber decorated, as shown in Fig. 2c. The aggregate carbon obtained ranged between 1.79 and 3.79 μm in size. The figure also depicts a smooth surface and some open pores network in the aggregate carbon ranging from 0.52 to 1.21 μm in size. Moreover, there are multilayer nanofibers onto the aggregate carbon surface and twig fiber structure, as shown by the marked region in Fig. 2d. The nanofiber had a diameter ranging from 65 to 119 nm. Initially, the carbon structure was modified by chemical activation. During the KOH-impregnated process, hemicellulose was extracted by alkaline, leaving numerous lignin and cellulose [55]. This

leads to the conversion of a sizeable aggregate structure into a small aggregate and nanofiber of ACH-3. Meanwhile, the chemical activation process also supports micropores formation [13, 38, 43]. KOH reacted with carbon atom during the carbonization process under the protection of inert gas. It produced main products, forming carbon, potassium, and potassium carbonate [43]. Additionally, some gases, including hydrogen, carbon dioxide, carbon monoxide, and water vapor were also produced and released at high temperatures [13, 38]. In the next stage, physical activation continuously enlarged the micropores and completely collapsed the walls between adjacent micropores to form larger pores [13, 43].

Furthermore, a higher concentration of KOH in the ACH-7 increased the number of the fiber and generated new pores onto the rough aggregate surface, as shown in Fig. 2e. Aggregate carbon and the open pores network were reduced in the range of 0.81–2.98 μm and 0.18–1.52 μm, respectively. There was a single structure nanofiber without twig and multilayers, as shown by the marked region in Fig. 2f. The nanofiber diameter was also reduced in the range of 51–89 nm. It also depicts that the new pores on the surface of aggregate carbon were formed. Initially, the increasing concentration of KOH produced more residual product which was K₂CO₃-occupied and K-bound at the high temperature [43]. This condition leaves numerous vacancies on the monolithic electrodes of ACH-7, either aggregate or nanofiber. It leads to generate more micropores onto the surface of aggregate carbon [13, 50, 51]. The physical activation at the high temperature of 900 °C enlarged the existed micropores into mesopores or macropores [13, 43]. Moreover, a higher concentration of KOH removed more hemicellulose and increased the degradations of lignin at the high temperature [55]. It rearranges the remaining carbon atom, increasing the number of the nanofiber but at the same time reducing their diameter. Finally, the residual product of activation was removed from the activated carbon by washing. Further, it predicts the aggregate fiber decorated in ACH-3 and ACH-7 had high specific surface area and electrochemical performance.

The N₂ adsorption/desorption isotherms were used to further analyze the specific surface area and pore structures in the carbon samples, as shown in Fig. 3a. All the samples exhibit the typical IV isotherm according to the international union of pure and applied chemists (IUPAC). The isotherm's significant increase in volume at the low relative pressure ($P/P_0 < 0.1$) indicates the presence of micropores [25, 39, 50]. The hysteresis loop at high relative pressure ($P/P_0 = 0.4–0.95$) indicates the presence of numerous mesopores [29, 31, 51]. Therefore, all the samples of ACH-X exhibit well-developed combination of micropores and mesopores. The isotherm of ACH-0 and ACH-7 shows normal hysteresis, which the adsorption/desorption is almost equal. It correlates with the SEM image (see Fig. 2a–b for

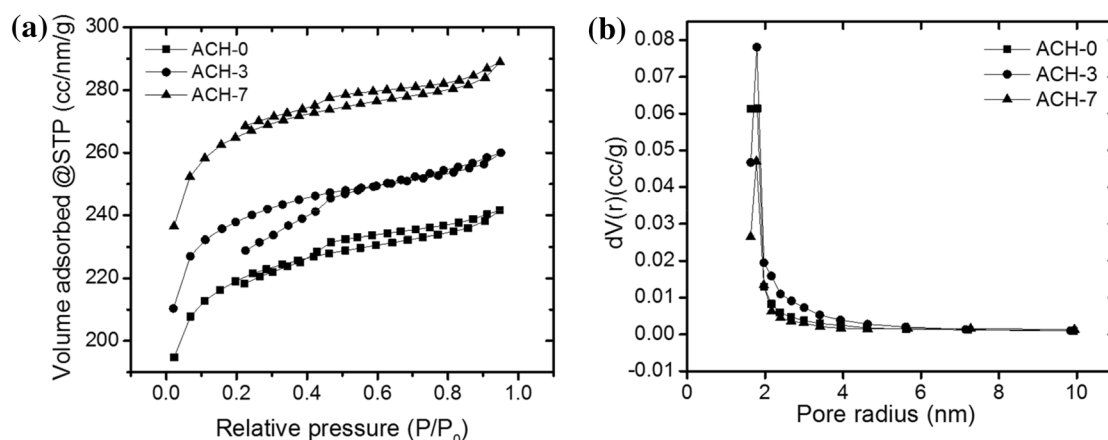


Fig. 3 Textural characteristic of ACH-X samples (a) Nitrogen adsorption–desorption isotherms (b) and pore size distribution

Table 1 The textural properties of ACH-X carbon samples

Samples	Specific surface area ($\text{m}^2 \text{g}^{-1}$)		Pore volume ($\text{cm}^3 \text{g}^{-1}$)		D_{average} (nm)
	S_{BET}	S_{BJH}	V_{TOTAL}	V_{BJH}	
ACH-0	696.689	35.300	0.375	0.040	2.136
ACH-3	754.974	41.712	0.403	0.050	2.151
ACH-7	838.636	23.642	0.448	0.032	2.137

ACH-0 and d–f for ACH-7), either macropores for ACH-0 or single layer nanofiber for ACH-7. Therefore, it reduces pore-blocking during the desorption process at low relative pressure. Furthermore, the isotherm of ACH-3 has unique hysteresis loop that displays a higher desorption volume than adsorption. This condition indicates the presence of unique textural in the ACH-3 samples. In reference to SEM image (see Fig. 2b–c), the ACH-3 displays the multilayer structure of nanofiber, blocking the desorption flow at low relative pressure [56]. Furthermore, the presence of a nanofiber structure suggests high specific surface area of ACH-X carbon samples.

The surface-specific area and pore structure parameter of all carbon samples are summarized in the Table 1. With increasing concentration of KOH in the electrodes from ACH-0, ACH-3, and ACH-7, the specific surface area (S_{BET}) increases from 696, 754, to 838 $\text{m}^2 \text{g}^{-1}$ with the total pore volume (V_{TOTAL}) of 0.375, 0.403, and 0.448 $\text{cm}^3 \text{g}^{-1}$, respectively. Additionally, the ACH-0, ACH-3, and ACH-7 have an average pore diameter of 2.136, 2.151, and 2.137 nm, respectively. As the alkali ratio in the carbon samples increases, the micropores formation also increases [50, 51]. As shown in Fig. 3b, the pore size distribution of ACH carbon samples were investigated by Barrett Joiner Halenda (BJH) model. The dominant pore sizes were 3.596, 3.528, 3.556 nm for ACH-0, ACH-3, and ACH-7, respectively. It was found that

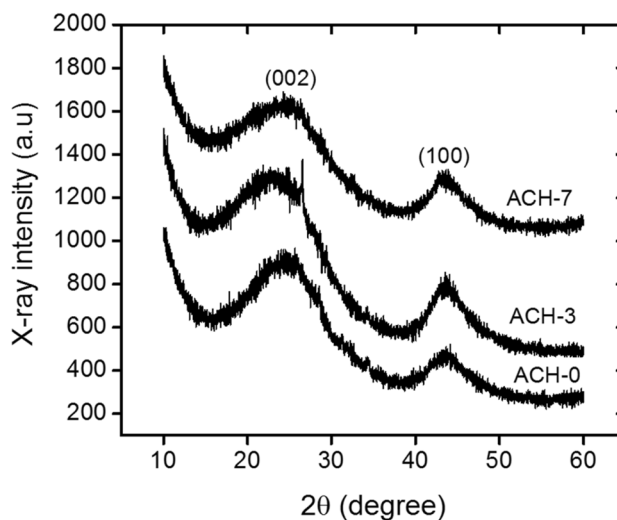


Fig. 4 XRD diffractogram of ACH-X samples

the pores size measured by BJH method were in the range of mesopore sizes (2–50 nm). Moreover, the surface area and total mesopore volume was obtained of 35.300, 41.712, 23.642 $\text{m}^2 \text{g}^{-1}$ and 0.040, 0.050, 0.032 $\text{cm}^3 \text{g}^{-1}$ for ACH-0, ACH-3, and ACH-7, respectively. In ACH-3 samples, using KOH as an activating agent followed by physical activation at high temperature enlarged micropores and increased mesopore [50]. The other hand, as increasing concentration of KOH in the ACH-7, it enlarged the existed micropores to macropores by collapsing the walls between their adjacent micropores [13]. The presence of macropores in carbon samples increases the ion diffusion rate to mesopore and micropores [23, 57]. It predicts the best performance for electrochemical performance.

XRD measurements were performed to confirm the crystalline structure of all samples. As shown in Fig. 4, the samples have two broad peaks at around 2θ angles, precisely 24°

and 44° for the carbon planes 002 and 100, respectively. The carbon planes of all samples ACH-X are the typical agreement with the amorphous structure of carbon materials [38], similar with carbon biomass from peanut shell [58], albizzia flower [41], peach gum [59]. The pyrolysis or carbonization process of carbon derived biomass materials obtained amorphous structure [60]. Furthermore, the amorphous carbon provides the porous carbon with the high porosity and large specific surface area [38]. The impure carbon of biomass materials shows the sharp peaks of the ACH-3 diffractogram. It has a high molecular weight that does not release high temperature for the activation process. In the ACH-3 samples, the presence of the impurity at around 2 θ angles 28° indicated a small amount of silica oxide (SiO₂) [24].

The lattice parameters, which include interlayer spacing (d_{002} and d_{100}) and microcrystalline (L_c for stack height and L_a for the stack width) structure were resumed in Table 2. The interlayer spacing was calculated using Bragg's Law ($n\lambda = 2d \sin 2\theta$), where n is diffraction order ($n = 1$), λ is the wavelength for the X-ray beam ($\lambda = 1.5406 \text{ \AA}$), and 2θ is the angles of XRD diffraction. The carbon planes from ACH-X samples have a good agreement with carbon materials at the interlayer spacing around 3.6 Å and 2.0 Å for 002 and 100, respectively. For example, activated carbon from empty fruit bunch of palm oil demonstrated a d_{002} between 3.692 and 3.711 Å [24]. The microcrystalline dimension was evaluated from Debye–Scherrer formula ($L_c = 0.89\lambda/\beta \cos(\theta_{002})$ and $L_a = 1.94\lambda/\beta \cos(\theta_{100})$), where β is equal to the peak width at half height [24, 61]. As shown in Table 2, the KOH activating agent have reduced L_c and increased L_a . The KOH activation in the high temperature supports to release the impurity and rearrangement of the carbon atom. The higher L_a for activated carbon may be caused by either sp^3 or interlayer repulsion, due to negatively charged of functional surface [61]. Furthermore, the ratio of L_c/L_a predicts the high porosity of ACH-X samples at a low ratio [24]. The L_c number affected the specific surface area in inverse correlation in Kumar empirical formula ($S = 2/(\rho L_c)$), where S is the predicted surface area, and ρ is the density of the graphite [62].

The EDS analysis reveals the chemical composition of ACH-X samples, which were resumed in Table 3. The integrated stage in both carbonization and physical activation successfully converts biomass into activated carbon of ACH materials. Activated carbon of ACH-X contains the carbon with an atomic weight of 85.12% for ACH-0. Generally, with

Table 3 Chemical composition analysis of ACH-X measured by EDS

Chemical contents	Atomic weight (%)		
	ACH-0	ACH-3	ACH-7
Carbon	85.12	90.59	89.34
Oxygen	11.11	7.68	8.46
Magnesium	0.35	0.20	0.23
Silica	2.28	1.07	1.17
Potassium	0.56	0.31	0.80
Chloride	–	0.15	–
Zinc	0.28	–	–
Sulfur	0.30	–	–
Total	100	100	100

chemical activation of KOH, the carbon content increased while oxygen decreased. The chemical activation of KOH etches the carbon-compounds bond, leading increase the carbon contained [43]. Meanwhile, low molecular weight and bad thermal stability at the high temperature limits the amount of oxygen released [29]. The increase in the concentration of KOH slightly decreased the carbon contents from 90.59% to 89.34% for ACH-3 and ACH-7, respectively. This is attributed to the increase in the oxygen contents from 7.68 to 8.46% for ACH-3 and ACH-7, respectively, which is the product of chemical and physical activation [5, 37]. However, the oxygen might contribute to be chemically absorbed in H₂O and/or C–OH, improving the hydrophilicity of electrode materials. For aqueous electrolyte, the hydrophilicity associated to ion adsorption from liquid electrolytes to the active specific surface area of electrode [25, 63]. It provides the best electrochemical performance for ACH-7, as predicted.

The Si is the common residual product that was obtained by the pyrolysis process for activated carbon fabrication derived biomass materials [29, 48, 64]. The other elements contained include magnesium and zinc, depending on the composition of cultivated soil [60]. A few amounts of the elements may remain after chemical and physical activation due to high molecular weight. The chloride can be obtained as the natural content of raw ACH-X, that could be released as gaseous phase at high temperature [38], depending on nominal composition. The other mineral in ACH-X activated carbon is sulfur, which can be removed by washing after chemical activation [60]. Potassium is the natural content of

Table 2 XRD parameters of all ACH-X samples

Samples	2 θ_{002} (°)	2 θ_{100} (°)	d_{002} (Å)	d_{100} (Å)	L_c (Å)	L_a (Å)	L_c/L_a (Å)
ACH-0	24.760	44.084	3.592	2.052	11.916	30.517	0.390
ACH-3	24.035	44.066	3.699	2.053	10.754	46.337	0.232
ACH-7	24.658	43.910	3.607	2.060	9.707	69.788	0.139

biomass [38], although it increases in the chemical activation of KOH due to imperfectly washing [48].

3.3 Electrochemical characteristic

ACH-X samples were prepared for working electrodes to investigate the capacitive performance using cyclic voltammetry (CV). ACH-X samples were assembled in the two-electrode system, and the CV tests were carried out in 1 M H_2SO_4 electrolyte at the scan rate of 1 mV/s, as shown in Fig. 5a. The CV curves depict the rectangular-like shape, which suggests the ideal double-layer capacitance of samples [31, 35]. In general, the CV curve area represents the charge–discharge rate, which determines the capacitance value.

The CV curve area of ACH-7 is largest for all ACH samples, which indicates that ACH-7 exhibits best electrochemical performance as predicted. In general, the specific capacitances (C_s) calculated from Eqs. (1) increase from 101.63, 117.31, and 120.24 to 181.96 F g^{-1} for ACH-0, ACH-3, and ACH-7, respectively, and drops for ACH-9 of 169.26 F g^{-1} . Notably, the increasing concentration of KOH in the ACH-X samples increased capacitance. For ideal specific capacitance, either the pores properties or carbon structure played critical roles in the storage and transport of electrolyte ions [71]. As discussed previously, the increasing concentration of KOH is attributed to expose the high SSA and the large number of pores volume. This condition provides sufficient active sites for ion pairs from both electrolyte ion and accessible surface area of activated carbon [31]. As the concentration of KOH increases in the ACH-9 samples, the pores structure may collapse and the SSA decreased. Table 4 shows the performance comparison of ACH with the biomass carbon based-nanofiber structure reported lasted, in the two-electrode system. It performs that ACH exhibits a high specific capacitance of 181.96 F g^{-1} .

As shown in Fig. 5b, ACH-7 depicts steady rectangular-like shapes of CV curves at different scan rates from 1 to 2 mV/s. This condition indicates that the ACH-7 has fast ion transport ability. As discussed previously, the open

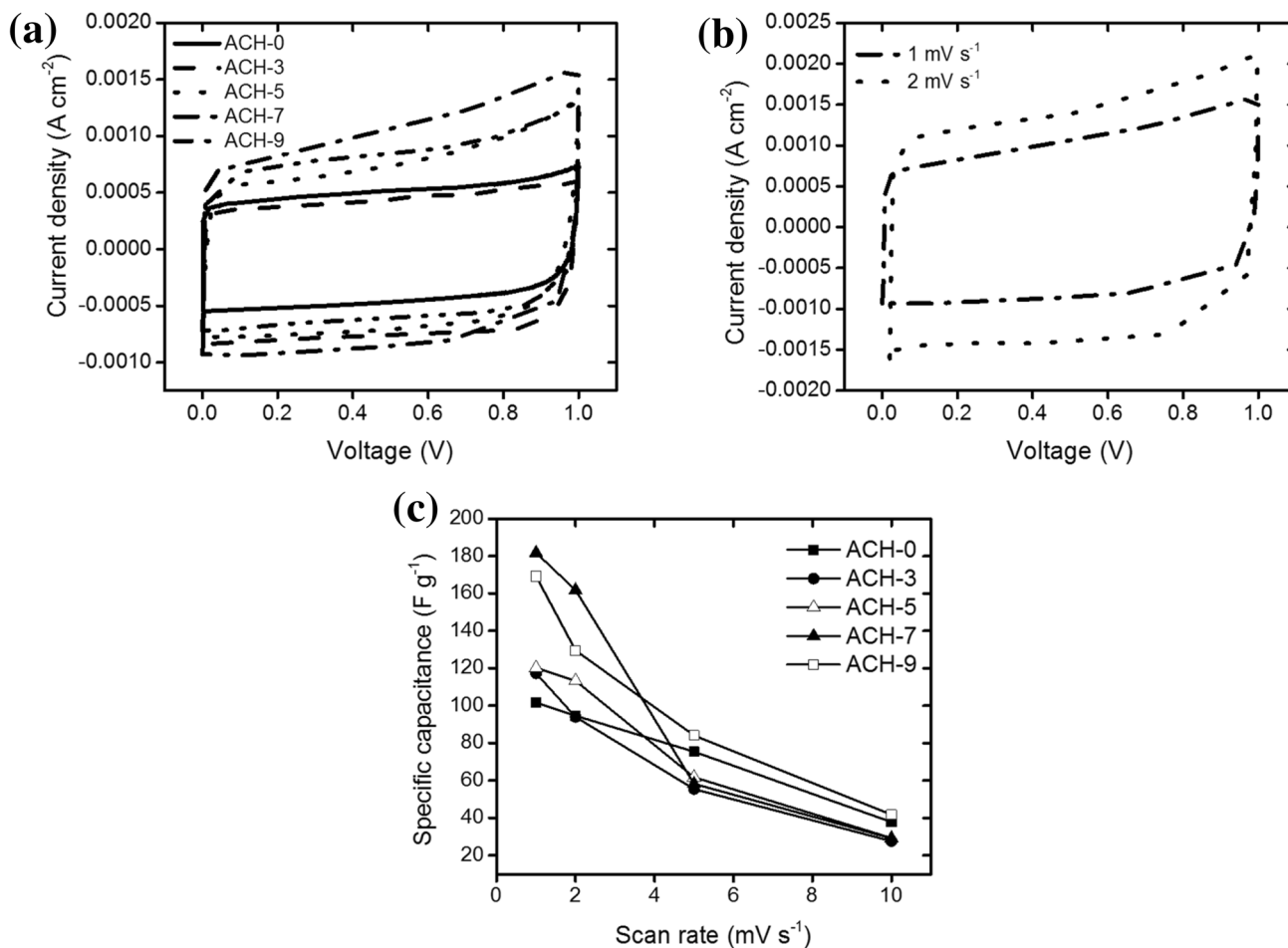


Fig. 5 Electrochemical measurements in a two-electrode system **a** CV curves of ACH-X samples at a scan rate of 1 mV/s **b** CV curve for ACH-7 at different scan rates **c** the specific capacitance of ACH-X samples at different scan rates

Table 4 Various precursors based-activated carbon as supercapacitor electrodes in two-electrodes system

Precursors	Nanofibers	Activator agent	S_{BET} ($\text{m}^2 \text{g}^{-1}$)	Cs (F g^{-1})	Electrolyte	Refs
Tea leaves	–	KOH	911	167	1 M Na_2SO_4	[25]
Albizia flower	–	KOH	2757	58	1 M Na_2SO_4	[41]
<i>Mangosteen</i> peels	–	KOH	1270	83	6 M KOH	[28]
Banana peels	–	KOH	1362	165	1 M NaNO_3	[65]
Dairy manure	–	KOH	1651	202	6 M KOH	[35]
Soybean	–	KOH	1749	116	0.5 M Na_2SO_4	[51]
Lumpy bracket	–	KOH	1968	223	6 M KOH	[61]
Waste tea	–	ZnCl_2	923	140	6 M KOH	[63]
<i>Setaria viridis</i>	–	KOH	701	199	6 M KOH	[66]
<i>Glebionis coronaria</i>	–	–	1007	205	6 M KOH	[67]
Starch	–	KOH	2259	81	2 M KOH	[68]
Orange peel	–	KOH	1577	168	6 M KOH	[69]
Corn leaf	–	H_3PO_4	2507	230	1 M H_2SO_4	[70]
<i>Areca catechu</i> husk	Nanofiber	KOH	839	182	1 M H_2SO_4	[This study]

pores network structure of ACH-7 can provide ion transport channels at high charge/discharge rates [23]. Furthermore, the micropores and mesopores of ACH-7 supplies a large amount of the accessible surface area for ion buffering and storage [25, 31]. In addition, the nanofiber structure of ACH-7 provide high SSA which ensure simply accessible interface for fast diffusion of electrolyte ions [14].

Calculated from CV curves at different scan rate, the specific capacitance of ACH-X samples were resumed as shown in Fig. 5c. The specific capacitance (C_s) of ACH-X samples decreases with the increase in the scan rate. The specific capacitance of ACH-0, ACH-3, ACH-5, ACH-7, and ACH-9 at the scan rate 2 mV/s slightly drops to 93.12, 80.09, 94.24, 89.00 and 76.53% of that at a scan rate of 1 mV/s, respectively. According to these results, the C_s value slightly decreases as the scan rate increase from 1 to 2 mV/s, implying that the ACH-X samples have a rapid ion transport to active SSA [23]. Furthermore, the unique trend of the C_s shows at the scan rate 5 to 10 mV/s, which significantly decreases for ACH-3, ACH-5, and ACH-7. From the previous discussion of morphology (see Fig. 2a–f), chemical activation using KOH increases the number of micropores formed. This is confirmed by the increase in the specific surface area and mesopore decrease (see Table 1). These conditions lead to an increase in the resistivity for ion diffusion, resulting low the C_s at high scan rate [25]. Meanwhile, the C_s of ACH-0 and ACH-9 is much higher than ACH-7. These results associated to better accessible SSA, provided by the larger open pores network between adjacent the aggregate for ACH-0, and the collapsing walls of the pores on the high KOH concentration for ACH-9. In addition, at the highest scan rate of 10 mV/s, it remains to be 37.27, 23.54, 24.31, 15.96, and 24.71%. It can be concluded that both the pores and unique structure of activated carbon electrode affects

ion diffusion to the active SSA, which determines the ion buffering and storage [71].

The ACH-X samples obtained the high energy densities of 14.11, 16.29, 16.70, 25.27, 23.50 Wh kg^{-1} for ACH-0, ACH-3, ACH-5, ACH-7, and ACH-9, respectively. While the power densities also were achieved of 50.86, 58.71, 60.18, 91, 07, 84.71 W kg^{-1} for each sample of ACH-0, ACH-3, ACH-5, ACH-7, and ACH-9. These results regard the energy and power density for activated carbon biomass electrodes. For example, activated carbon from lotus leaves exhibits the energy density between 25.76 and 30.28 Wh kg^{-1} and power density of 180 W kg^{-1} [31]. Activated carbon from soybean demonstrated the energy density of 12.5 Wh kg^{-1} and power density of 450 W kg^{-1} [51].

Therefore, it was found that the specific capacitance (C_s) value was affected by physical properties and chemical element, such as; (1) low density of pellet carbon electrode might provide high porosity for ion capturing; (2) a unique structure of nanofibers serves better surface accessibility and large specific surface area; (3) high specific surface area and large pore volume provides much ion pairs formation; (4) highly carbon composition indicates to high electrical conductivity of carbon electrode; (5) also, more oxygen content might contribute to increase the hydrophilicity degree for better ion adsorption in aqueous electrolyte; (6) highly disordered carbon atom by amorphous structure might generate the large surface of electrode, resulting high specific capacitance (C_s).

4 Conclusion

In summary, carbon nanofiber in monolith form were prepared from sustainable and green precursor *Areca catechu* husk (ACH) based cellulose microfibril through chemical

activation at different concentrations of KOH. Chemically activation of ACH samples transformed aggregate into nanofiber structure, by just one conventional route of integrated stage pyrolysis both carbonization and physical activation. The further chemical activation developed nanofiber structure, led to a large specific surface area and high pore volume, which is beneficial for achieving high electrochemical performance. Also, the optimized ACH-7 samples show a large specific surface area of $838.64 \text{ m}^2 \text{ g}^{-1}$ with a total pore volume of $0.448 \text{ cm}^3 \text{ g}^{-1}$. Symmetric supercapacitor fabricated from ACH-7 exhibits the highest specific capacitance of 181.96 F g^{-1} and maximum energy density of 25.27 Wh kg^{-1} for the power density of 91.07 W kg^{-1} in $1 \text{ M H}_2\text{SO}_4$ electrolyte. This study shows agreement the presence of nanofiber structure increases charge transfer and provides fast access for electrolyte ion into the surface of electrodes. This work provides a facile one conventional route of integrated pyrolysis to convert biomass *Areca catechu* husk into carbon nanofiber for high-performance electrode supercapacitor.

Acknowledgements This study was funded by DRPM Kemenristek-Dikti through second year Project of PD (396/UN.19.5.1.3/PT.01.03/2020) with the title “High-density micro-and nano carbon fiber made from biomass based materials for supercapacitor electrodes”.

References

- Zakeri B, Syri S (2015) Electrical energy storage systems: a comparative life cycle cost analysis. *Renew Sustain Energy Rev* 42:569–596. <https://doi.org/10.1016/j.rser.2014.10.011>
- Sovacool BK, Griffiths S (2019) The cultural barriers to a low-carbon future: a review of six mobility and energy transitions across 28 countries. *Renew Sustain Energy Rev* 119:109569. <https://doi.org/10.1016/j.rser.2019.109569>
- Koohi-Fayegh S, Rosen MA (2020) A review of energy storage types, applications and recent developments. *J Energy Storage* 27:101047. <https://doi.org/10.1016/j.est.2019.101047>
- Miller EE, Hua Y, Tezel FH (2018) Materials for energy storage: review of electrode materials and methods of increasing capacitance for supercapacitors. *J Energy Storage* 20:30–40. <https://doi.org/10.1016/j.est.2018.08.009>
- Faraji S, Nasir F (2015) The development supercapacitor from activated carbon by electroless plating—a review. *Renew Sustain Energy Rev* 42:823–834. <https://doi.org/10.1016/j.rser.2014.10.068>
- Tie D, Huang S, Wang J, Ma J, Zhang J, Zhao Y (2019) Hybrid energy storage devices: advanced electrode materials and matching principles. *Energy Storage Mater* 21:22–40. <https://doi.org/10.1016/j.ensm.2018.12.018>
- Karthick R, Chen F (2019) Free-standing graphene paper for energy application: progress and future scenarios. *Carbon* 150:292–310. <https://doi.org/10.1016/j.carbon.2019.05.017>
- Ghosh S, Santhosh R, Jeniffer S, Raghavan V, Jacob G, Nanaji K, Kollu P, Jeong SK, Grace AN (2019) Natural biomass derived hard carbon and activated carbons as electrochemical supercapacitor electrodes. *Sci Rep* 9:16315. <https://doi.org/10.1038/s41598-019-52006-x>
- Inagaki M, Konno H, Tanaike O (2010) Carbon materials for electrochemical capacitors. *J Power Sources* 195:7880–7903. <https://doi.org/10.1016/j.jpowsour.2010.06.036>
- Iqbal MZ, Zakar S, Haider SS (2020) Role of aqueous electrolytes on the performance of electrochemical energy storage device. *J Electroanal Chem* 858:113793. <https://doi.org/10.1016/j.jelechem.2019.113793>
- Ji H, Zhao X, Qiao Z, Jung J, Zhu Y, Lu Y, Zhang LL, Macdonald AH, Ruoff RS (2014) Capacitance of carbon-based electrical double-layer capacitors. *Nat Commun* 5:1–7. <https://doi.org/10.1038/ncomms4317>
- Gopiraman M, Deng D, Kim B, Chung I, Kim IS (2017) Three-dimensional cheese-like carbon nanoarchitecture with tremendous surface area and pore construction derived from corn as superior electrode materials for supercapacitors. *Appl Surf Sci* 409:52–59. <https://doi.org/10.1016/j.apsusc.2017.02.209>
- Yahya MA, Al-qodah Z, Ngah CWZ (2015) Agricultural bio-waste materials as potential sustainable precursors used for activated carbon production: a review. *Renew Sustain Energy Rev* 46:218–235. <https://doi.org/10.1016/j.rser.2015.02.051>
- Azwar E, Adibah W, Mahari W, Huang J (2018) Transformation of biomass into carbon nanofiber for supercapacitor application: a review. *Int J Hydrogen Energy* 43:20811–20821. <https://doi.org/10.1016/j.ijhydene.2018.09.111>
- Chen X, Timpe O, Hamid SBA, Schlogl R, Su DS (2008) Direct synthesis of carbon nanofibers on modified biomass-derived activated carbon. *Carbon* 47:313–347. <https://doi.org/10.1016/j.carbon.2008.11.001>
- Zhao X, Chen H, Kong F, Zhang Y, Wang S, Liu S, Lucia LA, Fatehi P, Pang H (2019) Fabrication, characteristics and applications of carbon materials with different morphologies and porous structures produced from wood liquefaction: a review. *Chem Eng J* 364:226–243. <https://doi.org/10.1016/j.cej.2019.01.159>
- Wang L, Yang G, Peng S, Wang J, Yan W, Ramakrishna S (2019) One-dimensional nanomaterials toward electrochemical sodium-ion storage applications via electrospinning. *Energy Storage Mater* 25:443–476. <https://doi.org/10.1016/j.ensm.2019.09.036>
- Kumar M, Hietala M, Oksman K (2019) Lignin-Based Electrospun Carbon Nanofibers. *Front Mater* 6:1–6. <https://doi.org/10.3389/fmats.2019.00062>
- Hassan MF, Sabri MA, Fazal H, Shahzad N, Hussain M (2019) Recent trends in activated carbon fibers production from various precursors and applications—a comparative review. *J Anal Appl Pyrolysis* 145:104715. <https://doi.org/10.1016/j.jaap.2019.104715>
- Su X, Li S, Jiang S, Peng Z, Guan X, Zheng X (2018) Superior capacitive behavior of porous activated carbon tubes derived from biomass waste-cottonier strobili fibers. *Adv Powder Technol* 29:2097–2107. <https://doi.org/10.1016/j.apt.2018.05.018>
- Danish M, Ahmad T (2018) A review on utilization of wood biomass as a sustainable precursor for activated carbon production and application. *Renew Sustain Energy Rev* 87:1–21. <https://doi.org/10.1016/j.rser.2018.02.003>
- Chang F, Yen S, Wang S (2018) Developing lignosulfonate-based activated carbon. *Fibers materials* 11:1877. <https://doi.org/10.3390/ma11101877>
- Wei X, Wei J, Li Y, Zou H (2019) Robust hierarchically interconnected porous carbons derived from discarded Rhus typhina fruits for ultrahigh capacitive performance supercapacitors. *J Power Sources* 414:13–23. <https://doi.org/10.1016/j.jpowsour.2018.12.064>
- Farma R, Deraman M, Awitdrus A, Talib IA, Taer E, Basri NH (2013) Preparation of highly porous binderless activated carbon electrodes from fibres of oil palm empty fruit bunches for application in supercapacitors. *Bioresour Technol* 132:254–261. <https://doi.org/10.1016/j.biortech.2013.01.044>

25. Song X, Ma X, Li Y, Ding L, Jiang R (2019) Tea waste derived microporous active carbon with enhanced double-layer supercapacitor behaviors. *Appl Surf Sci* 487:189–197. <https://doi.org/10.1016/j.apsusc.2019.04.277>
26. Faisal MSS, Abedin F, Asmatulu R (2020) Activated carbons of pistachio and acorn shells for supercapacitor electrodes with—TEABF₄/PC solutions as electrolytes. *Carbon Lett.* <https://doi.org/10.1007/s42823-020-00120-6>
27. Kumagai S, Tashima D (2015) Electrochemical performance of activated carbons prepared from rice husk in different types of non-aqueous electrolytes. *Biomass Bioenerg* 83:216–223. <https://doi.org/10.1016/j.biombioe.2015.09.021>
28. Li Y, Wang X, Cao M (2018) Three-dimensional porous carbon frameworks derived from mangosteen peel waste as promising materials for CO₂ capture and supercapacitors. *J CO₂ Util* 27:204–216. <https://doi.org/10.1016/j.jcou.2018.07.019>
29. Xue M, Lu W, Chen C, Tan Y, Li B, Zhang C (2019) Optimized synthesis of banana peel derived porous carbon and its application in lithium sulfur batteries. *Mater Res Bull* 112:269–280. <https://doi.org/10.1016/j.materresbull.2018.12.035>
30. Yu F, Ye Z, Chen W, Wang Q, Wang H, Zhang H, Peng C (2019) Plane tree bark-derived mesopore-dominant hierarchical carbon for high-voltage supercapacitors. *Appl Surf Sci* 507:145190. <https://doi.org/10.1016/j.apsusc.2019.145190>
31. Lu Q, Zhou S, Li B, Wei H, Zhang D, Hu J, Zhang J, Liu Q (2020) Mesopore-rich carbon flakes derived from lotus leaves and its ultrahigh performance for supercapacitors. *Electrochim Acta* 333:135481. <https://doi.org/10.1016/j.electacta.2019.135481>
32. Jiang W, Li L, Pan J, Senthil RA, Jin X, Cai J, Wang J, Liu X (2019) Hollow-tubular porous carbon derived from cotton with high productivity for enhanced performance supercapacitor. *J Power Sources* 438:226936. <https://doi.org/10.1016/j.jpowsour.2019.226936>
33. Zhang R, Gu X, Liu Y, Hua D, Shao M, Gu Z, Wu J, Zheng B, Zhang W, Li S, Huo F, Huang W (2020) Hydrophilic nano-porous carbon derived from egg whites for highly efficient capacitive deionization. *Appl Surf Sci* 512:145740. <https://doi.org/10.1016/j.apsusc.2020.145740>
34. Virtanen J, Pammo A, Keskinen J, Sarlin E, Tuukkanen S (2017) Pyrolysed cellulose nanofibrils and dandelion pappus in supercapacitor application. *Cellulose* 24:3387–3397. <https://doi.org/10.1007/s10570-017-1332-8>
35. Shen F, Su J, Zhu L, Qi X, Zhang X (2017) Comprehensive utilization of dairy manure to produce glucose and hierarchical porous carbon for supercapacitors. *Cellulose* 24:2571–2579. <https://doi.org/10.1007/s10570-017-1267-0>
36. Yang S, Cheng Y, Xiao X, Pang H (2020) Development and application of carbon fiber in batteries. *Chem Eng J* 384:123294. <https://doi.org/10.1016/j.cej.2019.123294>
37. Abioye AM, Abi FN (2015) Recent development in the production of activated carbon electrodes from agricultural waste biomass for supercapacitors: a review. *Renew Sustain Energy Rev* 52:1282–1293. <https://doi.org/10.1016/j.rser.2015.07.129>
38. Gonzalez-Garcia P (2018) Activated carbon from lignocellulosics precursors: a review of the synthesis methods, characterization techniques and applications. *Renew Sustain Energy Rev* 82:1393–1414. <https://doi.org/10.1016/j.rser.2017.04.117>
39. Ma X, Ding C, Li D, Wu M, Yu Y (2018) A facile approach to prepare biomass-derived activated carbon hollow fibers from wood waste as high-performance supercapacitor electrodes. *Cellulose* 25:4743–4755. <https://doi.org/10.1007/s10570-018-1903-3>
40. Tayeb P, Tayeb AH (2019) Nanocellulose applications in sustainable electrochemical and piezoelectric systems: a review. *Carbohydr Polym* 224:115149. <https://doi.org/10.1016/j.carbpol.2019.115149>
41. Wu F, Gao J, Zhai X, Xie M, Sun Y, Kang H, Tian Q (2019) Hierarchical porous carbon microrods derived from albizia flowers for high performance supercapacitors. *Carbon* 147:242–251. <https://doi.org/10.1016/j.carbon.2019.02.072>
42. Fic K, Platek A, Piwek J, Frackowiak E (2018) Sustainable materials for electrochemical capacitors. *Mater Today* 21:437–454. <https://doi.org/10.1016/j.mattod.2018.03.005>
43. Wang Y, Qu Q, Gao S, Tang G, Liu K, He S, Huang C (2019) Biomass derived carbon as binder-free electrode materials for supercapacitors. *Carbon* 155:706–726. <https://doi.org/10.1016/j.carbon.2019.09.018>
44. Chandra CJ, George N, Narayanankutty SK (2016) Isolation and characterization of cellulose nanofibrils from arecanut husk fibre. *Carbohydr Polym* 142:158–166. <https://doi.org/10.1016/j.carbpol.2016.01.015>
45. Kabir SMM, Dhar AK, Bhattacharjee M (2019) The use of natural Areca catechu dyes for silk and nylon and its halochromic effect. *J Text Inst.* <https://doi.org/10.1080/00405000.2019.1674542>
46. Binoj JS, Raj RE, Daniel BSS, Saravanakumar SS (2016) Optimization of short indian areca fruit husk fiber (Areca Catechu L.) reinforced polymer composites for maximizing the mechanical property. *Int J Polym Anal Charact* 5341:112–122. <https://doi.org/10.1080/1023666X.2016.1110765>
47. Devaki E, Sangeetha DK (2017) Extraction and characterisation of natural cellulosic husk fibre areca catechu. *Int J Res Appl Sci Eng Technol* 5:1468–1472. <https://doi.org/10.22214/ijras.et.2017.11212>
48. Taer E, Apriwandi HR, Taslim R, Awitdrus AA, Agustino II (2019) The synthesis of bridging carbon particles with carbon nanotubes from areca catechu husk waste as supercapacitor electrodes. *Int J Electrochem Sci* 14:9436–9448. <https://doi.org/10.20964/2019.10.34>
49. Taer E, Sugianto SMA, Taslim R, Iwantono DD, Deraman M (2014) Eggs shell membrane as natural separator for supercapacitor applications. *Adv Mater Res* 896:66–69. <https://doi.org/10.4028/www.scientific.net/AMR.896.66>
50. Huang G, Liu Y, Wu X, Cai J (2019) Activated carbons prepared by the KOH activation of a hydrochar from garlic peel and their CO₂ adsorption performance. *New Carbon Mater* 34:247–257. [https://doi.org/10.1016/S1872-5805\(19\)60014-4](https://doi.org/10.1016/S1872-5805(19)60014-4)
51. Lin G, Ma R, Zhou Y, Liu Q, Dong X, Wang J (2017) KOH activation of biomass-derived nitrogen-doped carbons for supercapacitor and electrocatalytic oxygen reduction. *Electrochim Acta* 261:49–57. <https://doi.org/10.1016/j.electacta.2017.12.107>
52. Zhao C, Huang Y, Zhao C, Shao X, Zhu Z (2018) Rose-derived 3D carbon nanosheets for high cyclability and extended voltage supercapacitors. *Electrochim Acta* 291:287–296. <https://doi.org/10.1016/j.electacta.2018.09.136>
53. Zhao N, Zhang P, Luo D, Xiao W, Deng L (2019) Direct production of porous carbon nanosheets / particle composites from wasted litchi shell for supercapacitors. *J Alloys Compd* 788:677–684. <https://doi.org/10.1016/j.jallcom.2019.02.304>
54. Yang X, Kong L, Cao M, Liu X, Li X (2020) Porous nanosheets-based carbon aerogel derived from sustainable rattan for supercapacitors application. *Ind Crops Prod* 145:112100. <https://doi.org/10.1016/j.indcrop.2020.112100>
55. Espinoza-acosta JL, Torres-chávez PI, Olmedo-martínez JL, Vega-rios A, Flores-gallardo S, Zaragoza-contreras EA (2018) Lignin in storage and renewable energy applications: a review. *J Energy Chem* 27:1422–1438. <https://doi.org/10.1016/j.jechem.2018.02.015>
56. Ayinla RT, Dennis JO, Zaid HM, Sanusi YK, Usman F, Adebayo LL (2019) A review of technical advances of recent palm bio-waste conversion to activated carbon for energy storage. *J Clean Prod* 229:1427–1442. <https://doi.org/10.1016/j.jclepro.2019.04.116>

57. Qiu Z, Wang Y, Bi X, Zhou T, Zhou J, Zhao J, Miao Z, Yi W, Fu P, Zhuo S (2018) Biochar-based carbons with hierarchical micro-meso-macro porosity for high rate and long cycle life supercapacitors. *J Power Sources* 376:82–90. <https://doi.org/10.1016/j.jpowsour.2017.11.077>
58. Murali G, Harish S, Ponnusamy S, Ragupathi J, Annal H (2019) Hierarchically porous structured carbon derived from peanut shell as an enhanced high rate anode for lithium ion batteries. *Appl Surf Sci* 492:464–472. <https://doi.org/10.1016/j.apsusc.2019.06.142>
59. Lin Y, Chen Z, Yu C, Zhong W (2020) Facile synthesis of high nitrogen-doped content, mesopore-dominated biomass-derived hierarchical porous graphitic carbon for high performance supercapacitors. *Electrochim Acta* 334:135615. <https://doi.org/10.1016/j.electacta.2020.135615>
60. Pallarés J, González-cencerrado A, Arauzo I (2018) Production and characterization of activated carbon from barley straw by physical activation with carbon dioxide and steam. *Biomass Bioenergy* 115:64–73. <https://doi.org/10.1016/j.biombioe.2018.04.015>
61. Serafin J, Baca M, Biegun M, Mijowska E, Kale RJ (2019) Direct conversion of biomass to nanoporous activated biocarbons for high CO₂ adsorption and supercapacitor applications. *Appl Surf Sci* 497:143722. <https://doi.org/10.1016/j.apsusc.2019.143722>
62. Kumar K, Saxena R, Kothari R, Suri D, Kaushik K, Bohra J (1997) Correlation between adsorption and X-ray diffraction studies on viscose rayon based activated carbon cloth. *Carbon* 35:1842–1844. [https://doi.org/10.1016/S0008-6223\(97\)87258-2](https://doi.org/10.1016/S0008-6223(97)87258-2)
63. Inal IIG, Aktas Z (2020) Enhancing the performance of activated carbon based scalable supercapacitors by heat treatment. *Appl Surf Sci* 514:145895. <https://doi.org/10.1016/j.apsusc.2020.145895>
64. Promdee K, Chanvidhwatanakit J, Satitkune S (2017) Characterization of carbon materials and differences from activated carbon particle (ACP) and coal briquettes product (CBP) derived from coconut shell via rotary kiln. *Renew Sustain Energy Rev* 75:1175–1186. <https://doi.org/10.1016/j.rser.2016.11.099>
65. Fasakin O, Dangbegnon JK, Momodu DY, Madito MJ, Oye-dotun KO, Eleruja MA, Manyala N (2018) Synthesis and characterization of porous carbon derived from activated banana peels with hierarchical porosity for improved electrochemical performance. *Electrochim Acta* 262:187–196. <https://doi.org/10.1016/j.electacta.2018.01.028>
66. Yan R, Wang K, Tian X, Li X, Yang T, Xu X, He Y, Lei S, Song Y (2019) Heteroatoms in situ-doped hierarchical porous hollow-activated carbons for high-performance supercapacitor. *Carbon Lett* 30:331–344. <https://doi.org/10.1007/s42823-019-00102-3>
67. Zhang Z, He J, Tang X, Wang Y, Yang B, Wang K, Zhang D (2019) Supercapacitors based on a nitrogen doped hierarchical porous carbon fabricated by self-activation of biomass: excellent rate capability and cycle stability. *Carbon Lett* 29:585–594. <https://doi.org/10.1007/s42823-019-00057-5>
68. Guo J, Guo H, Zhang L, Yang B, Cui J (2018) Hierarchically porous carbon as a high-rate and long-life electrode material for high-performance supercapacitors. *ChemElectroChem* 5:770–777. <https://doi.org/10.1002/celec.201701286>
69. Ahmed S, Rafat M, Ahmed A (2018) Nitrogen doped activated carbon derived from orange peel for supercapacitor application. *Adv Nat Sci* 9:035008. <https://doi.org/10.1088/2043-6254/aad5d4>
70. Yang X, Li C, Chen Y (2017) Hierarchical porous carbon with ultrahigh surface area from corn leaf for high-performance supercapacitors application. *J Physic D* 50:055501. <https://doi.org/10.1088/1361-6463/50/5/055501>
71. Chen D, Li L, Xi Y, Li J, Lu M, Cao J, Han W (2018) Self-assembly of biomass microfibers into 3D layer-stacking hierarchical porous carbon for high performance supercapacitors. *Electrochim Acta* 286:264–270. <https://doi.org/10.1016/j.electacta.2018.08.030>

Publisher's Note Springer Nature remains neutral with regard to jurisdictional claims in published maps and institutional affiliations.